Numerical simulations of energy deposition caused by 50 MeV—50 TeV proton beams in copper and graphite targets

Y. Nie,[1,*] R. Schmidt,[1] V. Chetvertkova,[2] G. Rosell-Tarragó,[3] F. Burkart,[1] and D. Wollmann[1]
[1]*CERN, CH-1211 Geneva 23, Switzerland*
[2]*GSI Helmholtzzentrum für Schwerionenforschung, Planckstraße 1, 64291 Darmstadt, Germany*
[3]*University of Barcelona, Martí i Franquès 1, 08028 Barcelona, Spain*
(Received 28 April 2017; published 9 August 2017)

The conceptual design of the Future Circular Collider (FCC) is being carried out actively in an international collaboration hosted by CERN, for the post–Large Hadron Collider (LHC) era. The target center-of-mass energy of proton-proton collisions for the FCC is 100 TeV, nearly an order of magnitude higher than for LHC. The existing CERN accelerators will be used to prepare the beams for FCC. Concerning beam-related machine protection of the whole accelerator chain, it is critical to assess the consequences of beam impact on various accelerator components in the cases of controlled and uncontrolled beam losses. In this paper, we study the energy deposition of protons in solid copper and graphite targets, since the two materials are widely used in magnets, beam screens, collimators, and beam absorbers. Nominal injection and extraction energies in the hadron accelerator complex at CERN were selected in the range of 50 MeV–50 TeV. Three beam sizes were studied for each energy, corresponding to typical values of the betatron function. Specifically for thin targets, comparisons between FLUKA simulations and analytical Bethe equation calculations were carried out, which showed that the damage potential of a few-millimeter-thick graphite target and submillimeter-thick copper foil can be well estimated directly by the Bethe equation. The paper provides a valuable reference for the quick evaluation of potential damage to accelerator elements over a large range of beam parameters when beam loss occurs.

DOI: 10.1103/PhysRevAccelBeams.20.081001

I. INTRODUCTION

The Large Hadron Collider (LHC) has recently reached three new performance records: unprecedented peak luminosity, number of proton bunches, and beam lifetime. In order to further extend the discovery potential of the LHC, it will be upgraded to the High Luminosity LHC (HL-LHC) around the year 2025 to increase its annual integrated luminosity by a factor of 10 [1]. A higher-energy LHC (HE-LHC) is also considered to approach a beam energy of 16.5 TeV corresponding to a 20 T dipole magnet field in the same LHC tunnel [2]. Note that the nominal LHC parameters are 7 TeV and 8.33 T, correspondingly. The target peak luminosity of the HE-LHC is 2×10^{34} cm^{-2} s^{-1}, twice the LHC design luminosity. Meanwhile, several high-energy colliders are currently at their conceptual design or planning stage in the world, including the International Linear Collider (ILC) [3], the Compact Linear Collider (CLIC) [4], the Circular Electron Positron Collider (CEPC) [5], and the Future Circular Collider (FCC) [6,7]. It is worth mentioning that the CEPC has the potential to be upgraded to a Super Proton-Proton Collider (SPPC) in the same 50–100 km tunnel with a center-of-mass energy between 70 and 140 TeV. The FCC study puts an emphasis on a circular proton-proton collider (FCC-hh) and an electron-positron collider (FCC-ee). For the FCC-hh, each of the two counterrotating proton beams will be accelerated up to 50 TeV in the proposed 100 km tunnel located in the Lake Geneva basin. A main dipole field of 16 T is necessary to deflect the beams accordingly. This frontier machine will deliver a peak luminosity of $5–30 \times 10^{34}$ cm^{-2} s^{-1}, and hence a total integrated luminosity of 17.5 ab^{-1} in a 25 year operating period is foreseen. The FCC conceptual study is being carried out in a global collaboration of more than 70 institutes hosted by CERN.

In high-energy colliders, especially the hadron-hadron colliders, energies stored in circulating beams are impressive. For instance, the energy stored in one nominal FCC-hh beam is 8500 MJ, which is more than 20 times the energy of today's LHC beam and sufficient to melt 12 t of copper when heated up from room temperature. Any uncontrolled release of the beam energy could result in severe damage to the accelerator equipment. Therefore, the safe operation of high-energy colliders highly relies on robust machine protection systems [8,9]. In the LHC machine protection system, collimators are responsible to

*Corresponding author.
yuancun.nie@cern.ch

clean the beam halo via both momentum collimation and betatron collimation by defining the aperture during routine operation, so that beam-induced quenches of the superconducting magnets can be avoided to the maximum extent. Dedicated beam absorbers and collimators provide passive protection against abnormal beam losses that arise extremely fast during, e.g., injection or extraction. Fast and reliable instrumentation and beam monitoring systems detect actively element failures and abnormal beam parameters (for example, beam loss rate) that are able to trigger a beam dump request before damage thresholds are reached. Beam interlock systems provide the highly reliable transmission of the dump request from the monitoring system to a beam dumping system. The beam dumping system waits for the particle-free abort gap for switching on the extraction kicker magnets (i.e., synchronous beam dump), extracts the beam from the ring in a single turn, dilutes the energy density, and disposes the beam onto a beam dump block that is designed to withstand the impact of the full beam. As can be seen, it is essential to study the interaction of these high-energy and high-intensity beams with matter to design a properly functioning machine protection system, with regard to regular and accidental particle losses.

Different scenarios of beam loss due to operating and failure modes need to be considered. The worst case is when the entire beam impacts on a single point; then the so-called hydrodynamic tunneling effect can be important. With a beam composed of a long bunch train, energy deposited by a certain number of head bunches produces an outgoing radial shock wave which reduces the density along and around the beam axis in the target. The subsequent bunches and their hadronic shower penetrate deeper and deeper into the target. However, the likelihood of such a failure is rather low. In this paper, we put an emphasis on less-severe beam losses that have a much higher probability to occur, such as proton losses in the beam (e.g., halo particles) at aperture limitations in the accelerator, beam losses during asynchronous beam dump and when injecting a low-intensity pilot bunch into an empty machine, etc. The injection of pilot bunches is an operational procedure for the LHC to ensure that all parameters are correctly set. Only when pilot bunches are circulating in the LHC can a higher-intensity beam be injected. For these beam losses, the calculation of the energy deposition is sufficient to understand if accelerator components could be damaged.

For the sake of more general interest, we first briefly summarize the existing studies on the hydrodynamic tunneling. For a failure scenario where the energy deposition of a bunch train impacting on material exceeds vaporization, an approach coupling a particle shower simulation code and a hydrodynamic code is required. The first time this has been done is for the SSC [10]. In the past few years, some of the worst possible failure scenarios were studied for the Super Proton Synchrotron (SPS) [11–13] and the LHC [14–18] by some of us (Schmidt, Burkart, and Wollmann) together with other collaborators. Hydrodynamic tunneling leads to a remarkable range lengthening of the proton energy deposition. The fully integrated particle physics Monte Carlo simulation package FLUKA [19–21] was employed to obtain the energy deposition distribution of protons in the target, while the two-dimensional hydrodynamic code BIG2 was used to simulate the thermodynamic and hydrodynamic response of the target material. BIG2 uses the energy deposition data from FLUKA as input, while FLUKA needs the modified target density distribution from BIG2 to calculate the new energy deposition map which again serves as the input of BIG2. The interaction of the entire beam (bunch train) with the target is thus simulated iteratively. Dedicated experiments performed at the High-Radiation to Materials (HiRadMat) facility applying the 440 GeV SPS proton beam have confirmed the existence of the hydrodynamic tunneling and validated the numerical simulation strategy [22–25]. Most recently, a simulation study has illustrated that the 50 TeV FCC beam will penetrate about 350 m in copper [26,27]. Table I summarizes the existing quantitative studies of hydrodynamic tunneling induced by high-energy and high-intensity proton beams from the SPS, the LHC, and the FCC in copper and graphite. The targets were homogeneous cylinders. A density of 2.28 g/cm^3 was used for graphite in Ref. [18]. A bunch length of 0.5 ns was adopted for all the cases. In these studies, no suitable scaling method was suggested to predict the tunneling range when changing parameters such as the beam size or beam energy, since the hydrodynamic tunneling effect is a complex nonlinear problem coupling multiphysics. Dedicated numerical or experimental studies are needed for specific cases. However, for an order-of-magnitude estimation, Table I provides many useful references.

For most of the cases of less-severe beam loss, it is adequate to make an order-of-magnitude estimation of the beam impacts according to the energy deposition data in solid targets only, since the hydrodynamic tunneling becomes less significant. The design and operation of a machine protection system is usually conservative with respect to the calculated damage level. Therefore, it is very helpful to have an overall knowledge of the energy deposition features in typical materials like copper and graphite on hand, for representative beam energies and beam sizes. Based on such data, rough (but frequently adequate) estimations can be performed quickly and conveniently relating to beam-related machine protection issues, especially for on-site support. Considering that in the existing literature the samples of beam energy and beam size are rather limited, we have simulated and analyzed the energy deposition characteristics of protons in copper and graphite for various beam sizes at energies in the range from 50 MeV to 50 TeV to cover the entire CERN hadron accelerator complex from the Linear accelerator 2

TABLE I. Summary of hydrodynamic tunneling studies for the SPS, the LHC, and the FCC.

Accelerator	Proton energy	Bunch number	Bunch intensity	Bunch separation	rms beam size	Target material	Tunneling range	Source
SPS	440 GeV	108	1.5×10^{11}	50 ns	0.2 mm	Copper	0.8 m	Simulation [23]
SPS	440 GeV	108	1.5×10^{11}	50 ns	0.2 mm	Copper	0.795 m	Experiment [24,25]
SPS	440 GeV	144	1.5×10^{11}	50 ns	0.2 mm	Copper	0.9 m	Simulation [23]
SPS	440 GeV	144	1.5×10^{11}	50 ns	0.2 mm	Copper	0.85 m	Experiment [24,25]
SPS	450 GeV	288	1.1×10^{11}	25 ns	0.088 mm	Copper	1.3 m	Simulation [11]
SPS	440 GeV	288	1.15×10^{11}	25 ns	0.2 mm	Copper	1.1 m	Simulation [22]
SPS	440 GeV	288	1.15×10^{11}	25 ns	0.5 mm	Copper	0.85 m	Simulation [18,22]
LHC	7 TeV	2808	1.15×10^{11}	25 ns	0.2 mm	Copper	35 m	Simulation [13,17]
LHC	7 TeV	2808	1.15×10^{11}	25 ns	0.5 mm	Graphite	25 m	Simulation [18]
FCC	40 TeV	10600	1.0×10^{11}	25 ns	0.2 mm	Copper	290 m	Simulation [27]
FCC	50 TeV	10600	1.0×10^{11}	25 ns	0.2 mm	Copper	350 m	Simulation [27]

(LINAC2), to the Proton Synchrotron Booster (PSB), the Proton Synchrotron (PS), the SPS, the LHC, and the FCC.

In Sec. II, the CERN hadron accelerator complex will be briefly described. Studies on the energy deposition of protons in a solid copper target will be presented in Sec. III, including FLUKA simulations and a comparison with the analytical results obtained via the Bethe equation in the case of a thin target. In Sec. IV, we will show the corresponding results for a graphite target. Conclusions drawn from this work will be given In Sec. V.

II. HADRON ACCELERATOR COMPLEX AT CERN

The schematic view of the CERN accelerator complex is shown in Fig. 1. LINAC2 is the starting point for the proton accelerators at CERN, providing 100 μs proton pulses up to 50 MeV at a maximum average pulse current of 160 mA to the PSB [28]. In order to double the brightness and intensity of the beam from the PSB, and hence break the space-charge-dominated bottleneck towards higher brightness of the LHC, LINAC2 will be replaced by LINAC4 in the near future [29]. LINAC4 will deliver an H^- beam at

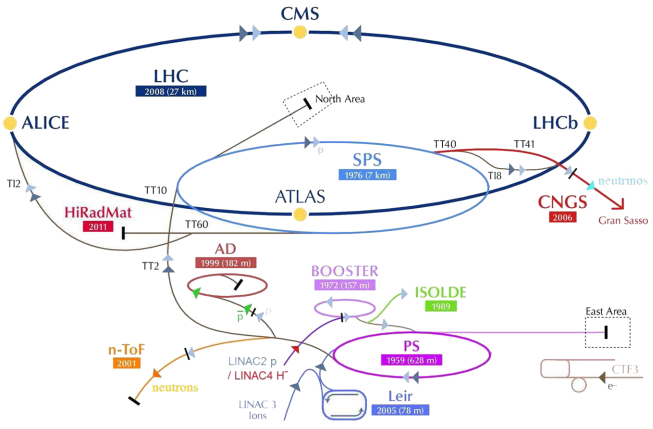

FIG. 1. Schematic view of the CERN accelerator complex.

160 MeV with a pulse length of 400 μs and up to 40 mA pulse current. The PSB is made up of four superimposed rings that accelerate the 50 MeV protons to 1.4 GeV for injection into the PS [30,31]. For the nominal operating mode of the LHC, the four PSB rings supply a total of six bunches in two batches for the PS. The six bunches fill six out of seven buckets in the PS working on rf harmonic $h = 7$. They are first divided into 18 bunches on $h = 21$ by a triple splitting and then accelerated up to 26 GeV, where each bunch is twice split in two to produce 72 consecutive bunches spaced by 25 ns on $h = 84$. A 300 ns gap in the bunch train is left for the rising time of the PS extraction kicker and the SPS injection kicker. To reach the nominal bunch intensity of 1.15×10^{11} at the LHC, each bunch from the PS must contain 1.35×10^{11} protons, meaning that one bunch from the PSB rings should have more than 16.2×10^{11} protons. The 6.9 km long SPS is capable of accelerating protons from 26 to 450 GeV. As the injector of the LHC, the SPS has up to 288 bunches and a total number of protons of 3.3×10^{13}, i.e., about 1.15×10^{11} protons per bunch. Two counterrotating proton beams at an energy up to 7 TeV then collide at four interaction regions in the 26.7 km long LHC tunnel. Each LHC beam comprises of up to 2808 bunches with 1.15×10^{11} protons per bunch. The energy stored in one beam is thus 362 MJ that is sufficient to melt 500 kg of copper.

As mentioned earlier, a conceptual study of the FCC is currently being carried out. The goal of the FCC-hh is to provide proton-proton collisions at a center-of-mass energy of 100 TeV, nearly an order of magnitude higher than the LHC. Each beam has 10600 bunches spaced by 25 ns, and every bunch consists of 1.0×10^{11} protons that will be accelerated up to 50 TeV in the new 100 km tunnel. One injection scheme is making use of the existing LHC as an injector which provides 3.3 TeV proton bunches for the FCC. The rms bunch length is about 0.3 ns, similar to the LHC. The designed normalized rms emittance of the FCC will be 2.2 μm, compared to 3.75 μm (nominal) of the

TABLE II. Typical parameters of the CERN hadron accelerator complex.

Accelerator	PSB	PS	SPS	LHC	FCC
Injection energy	50 MeV	1.4 GeV	26 GeV	450 GeV	3.3 TeV
Extraction energy	1.4 GeV	26 GeV	450 GeV	7 TeV	50 TeV
Number of bunches	1/ring	72	288	2808	10600
Bunch intensity	16.2×10^{11}	1.35×10^{11}	1.15×10^{11}	1.15×10^{11}	1.0×10^{11}
Beam energy	0.4 kJ	40 kJ	2.4 MJ	362 MJ	8500 MJ
Normalized emittance	2.5 μm	3 μm	3.5 μm	3.75 μm	2.2 μm
Pulse length	~190 ns (per bunch)	1.8 μs	7.2 μs	88.9 μs	327 μs
Circumference	157 m (four rings) 1/4 PS	628 m 1/11 SPS	6.9 km 7/27 LHC	26.7 km 3/11 FCC	97.97 km 11/3 LHC

LHC. The most relevant parameters of the above accelerators are listed in Table II.

We assume that the proton beam has a Gaussian distribution in both transverse planes. The horizontal and vertical rms beam size is determined by $\sigma = \sqrt{\beta_b \varepsilon_{n,rms}/\beta\gamma}$, where β_b is the betatron function depending on the beam optics, $\varepsilon_{n,rms} = \beta\gamma\varepsilon_{rms}$ is the normalized rms emittance, $\beta = v/c$ is the relative velocity, and $\gamma = 1/\sqrt{1-\beta^2}$ is the ratio of the total energy to the rest energy of a particle. For the nominal 450 GeV SPS beam, $\varepsilon_{n,rms}$ is about 3.5 μm. Assuming an average betatron function of $\beta_b = 100$ m, the beam size is $\sigma = 0.85$ mm. For the LHC, $\varepsilon_{n,rms} = 3.75$ μm and a betatron function of 100 m yield a beam size of $\sigma = 0.22$ mm at 7 TeV. In the case of the 50 TeV FCC beam, $\varepsilon_{n,rms} = 2.2$ μm, the beam size will be 0.09 mm with a betatron function of 200 m. The typical beam size at the LINAC2, PSB, and PS is up to a few millimeters. From the viewpoint of machine protection, we considered the worst case scenarios. Therefore, we first studied the case where the beam size was kept to be 0.2 mm for all the energies. Additionally, two other typical beam sizes were investigated depending on the beam energy, which can be found in Table III of Sec. III.

III. ENERGY DEPOSITION OF PROTON IN SOLID COPPER

In this section, we first introduce the FLUKA code and the simulation settings. The simulated energy deposition per proton corresponding to a variety of beam parameters in a solid copper target will then be shown in detail. A comparison between the simulated energy deposition and the energy loss from analytical calculations using the Bethe equation is performed in the case of thin targets. Moreover, the specific energy deposition of bunched protons and their effect on copper targets are presented.

A. FLUKA code and simulation setup

Protons that are incident on the target material produce particle cascades that deposit their energy inside the target, leading to an increase of the target temperature. The beam parameters together with the specific heat capacity of the material determine the temperature increase. In this paper, the FLUKA code [19–21] is used to calculate the interaction between protons and copper, assuming solid copper density. FLUKA is a multipurpose Monte Carlo simulation tool for calculations of particle transport and interactions with matter. Its applications cover an extended range from proton and electron accelerator shielding to target design, activation, detector design, dosimetry, accelerator-driven systems, radiotherapy, etc. FLUKA is capable of simulating with high accuracy the interaction and propagation in matter of about 60 different particles, including photons and electrons from 100 eV to 1 keV to thousands of TeV, neutrinos, muons of 1 keV to 1000 TeV, hadrons of energies from keV up to 10 PeV and all the corresponding antiparticles, neutrons from 10 PeV down to thermal energies, and heavy ions. Note that FLUKA should be linked with the DPMJET code via the integrated interface at hadron or neutron energies higher than 20 TeV. In our simulation, the Monte Carlo event generator DPMJET-III was linked, which is based on the dual parton model and unifies all features of the DTUNUC-2, DPMJET-II, and PHOJET1.12 event generators. It hence allows the simulation of hadron-hadron, hadron-nucleus, nucleus-nucleus, photon-hadron, photon-photon, and photon-nucleus interactions from a few GeV up to the highest cosmic ray energies [32]. The detailed transport limits of secondary particles and primary particles, the models applied in FLUKA, and the benchmarking can be found in Refs. [19–21].

The geometry adopted in the FLUKA simulations was a cylinder of solid copper with a radius of the order of 1 cm and a length up to a few meters depending on the beam energy and beam size. The protons were projected perpendicularly to the front face of the target, and the energy deposition distribution was calculated under a circular symmetry condition. Default values for precision simulations were set in the FLUKA input file, where, for example, the delta ray production (with threshold 100 keV) and transport were switched on [19,21]. Neither momentum spread nor beam divergence was considered. In every simulation, FLUKA took a primary particle from the predefined beam, started the transport, and repeated until the predetermined number of primary histories was reached. The equivalent number of primaries was typically more than 10^4 in order to control the relative statistical error

below a few percent. Finally, the energy deposition per proton in the beam was obtained. Geometry-dependent scoring was performed to score the spatial distribution of the energy deposition in a regular mesh (binning). We spanned the angular coordinate $0 < \Phi < 2\pi$ in one bin, since the circular symmetry condition was met in the cylindrical coordinates assuming the horizontal and vertical beam sizes are always the same. The radial bin size was adjusted to be one-quarter of one rms beam size σ, whereas in the longitudinal direction, the bin size was increased as the beam energy went from 50 MeV to 50 TeV and correspondingly the shower range became larger and larger. The longitudinal bin size was 0.005 cm at 50 MeV, 0.01 cm at 160 MeV, 0.4 cm at 1.4 GeV, and 0.5 cm at 26 GeV and all higher energies.

B. Simulated energy deposition per proton

Figures 2(a) and 2(b) show the two-dimensional energy deposition distributions corresponding to a beam size of $\sigma = 0.2$ mm at 50 MeV and 50 TeV, respectively. In addition to substantially different interaction ranges, the behaviors show a large variance. In the case of 50 MeV, the proton releases its majority of energy in the target around the position of $L = 0.39$ cm, implying the existence of the Bragg peak. For 50 TeV, there is no such apparent peak, and most of the beam energy is deposited spanning a relatively wide region around $L = 22$ cm in the target.

Figure 3(a) presents the energy deposition per 50 MeV proton in copper along the target axis (also the beam axis), for Gaussian beams with beam sizes of 0.2, 0.4, and 1.0 mm, respectively. The energy deposition at the Bragg peaks is 75.4, 30.4, and 6.0 GeV/(cm^3 p), respectively. The corresponding radial profiles at $L = 0.39$ cm (position of the Bragg peaks) are plotted in Fig. 3(b). It is seen that the deposited energy attenuates rapidly with an increasing radius.

For 50 TeV, the energy deposition distributions in the longitudinal direction and radial direction are shown in Figs. 4(a) and 4(b), respectively. Without sharp peaks, the maximum energy deposition for the beam size of 0.1 mm is 19326.6 GeV/(cm^3 p) at $L = 21.3$ cm, for 0.2 mm, 9736.3 GeV/(cm^3 p) at $L = 22.3$ cm, and for 0.4 mm, 5043.6 GeV/(cm^3 p) at $L = 23.8$ cm. It can be seen that the maximum value reduces approximately by half as the

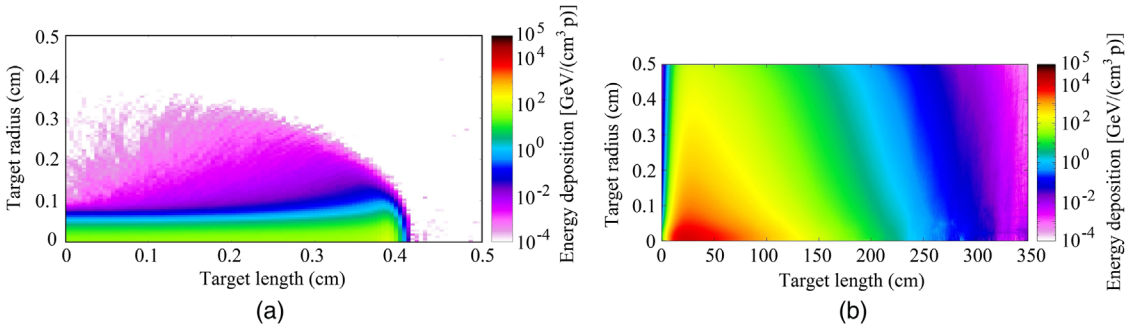

FIG. 2. Two-dimensional energy deposition in the units of GeV/cm^3 per proton in a solid copper target at the energies of (a) 50 MeV and (b) 50 TeV. The rms beam size is $\sigma = 0.2$ mm.

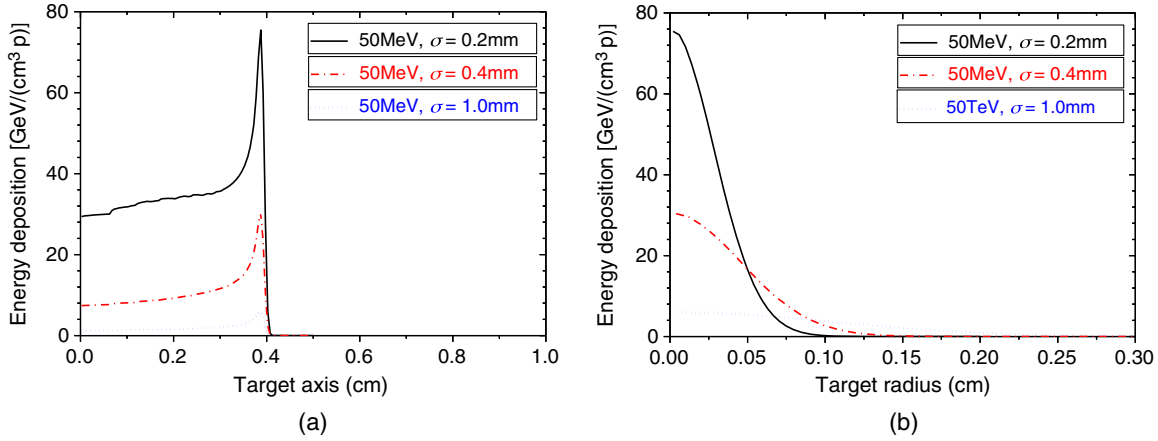

FIG. 3. Energy deposition per 50 MeV proton in a cylindrical copper target for three different beam sizes (a) in the longitudinal direction at $r = 0$ and (b) in the radial direction at $L = 0.39$ cm (position of the Bragg peaks). The three beam sizes are 0.2, 0.4, and 1.0 mm.

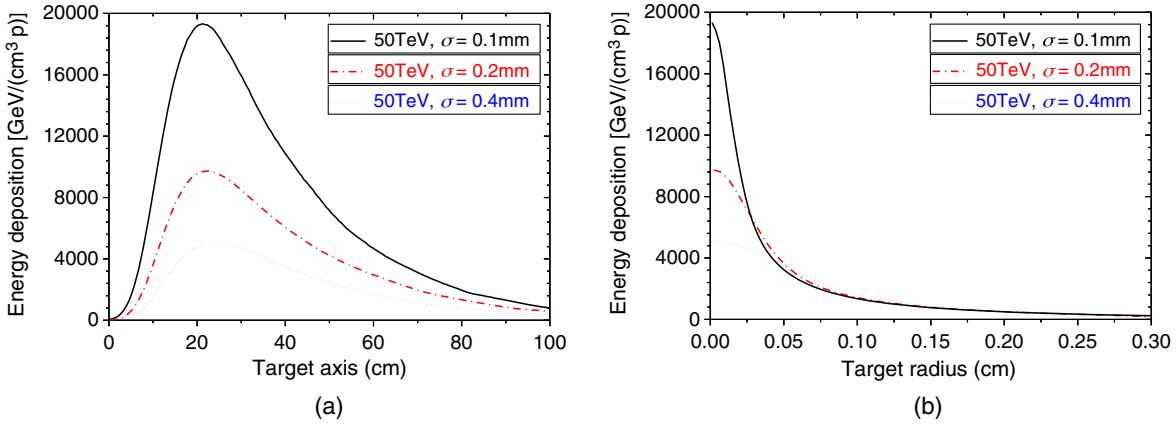

FIG. 4. Energy deposition per 50 TeV proton in a cylindrical copper target for three different beam sizes (a) in the longitudinal direction at $r = 0$ and (b) in the radial direction at $L = 21.3$ cm for the beam size of 0.1 mm, $L = 22.3$ cm for 0.2 mm, and $L = 23.8$ cm for 0.4 mm, where we have the maximum energy deposition.

beam size is doubled. The peak occurs slightly deeper in the target as the beam size grows.

In Fig. 5, we plot the energy deposition as a function of the depth into the solid copper target along the axis. In the FLUKA simulations, the beam size was kept to be 0.2 mm over 6 orders of magnitude in proton energy, from 50 MeV to 50 TeV. As can be seen, these curve properties for various energies are dramatically different. The length influenced by the incident primary proton increases from a few millimeters up to a few meters as the energy becomes higher and higher. The Bragg peak is high at 50 MeV, whereas at 160 MeV, it becomes relatively low compared to the overall energy deposition. At energies higher than 1.4 GeV, the Bragg peak disappears, covered by the energy deposition from the secondary particles which lead to wide

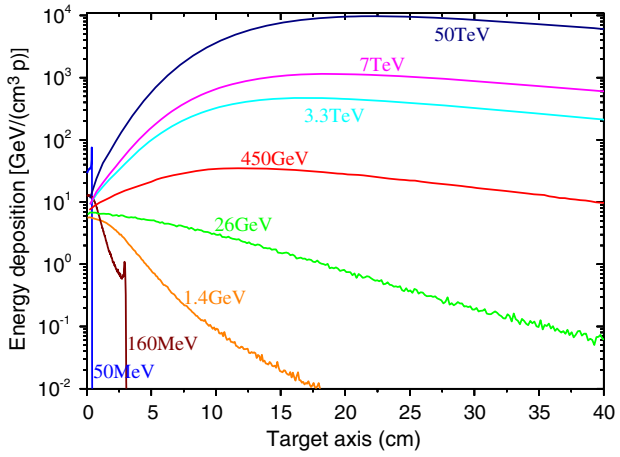

FIG. 5. Energy deposition per incident proton as a function of the depth into the solid copper target at $r = 0$. The beam size is constant (0.2 mm) for the energies from 50 MeV to 50 TeV. It is interesting to note that the results shown here are significantly higher than that reported in Ref. [33]. We have clarified that this is mainly due to the coarse bin settings (large scoring steps) in the previous work.

maxima. The maxima occur close to the entrance at both 1.4 and 26 GeV. As the energy increases from 450 GeV to 50 TeV, the maximum moves deeper and deeper from 12.6 to 22.3 cm. The maximum energy deposition is 75.4 GeV/(cm^3 p) at 50 MeV ($\beta\gamma = 0.33$), falls to a minima of 5.7 GeV/(cm^3 p) at 1.4 GeV ($\beta\gamma = 2.28$), and then rises to 9736.3 GeV/(cm^3 p) at 50 TeV ($\beta\gamma = 53291.1$), as shown in Fig. 6.

At 50 TeV, the energy deposition along the target axis was also simulated while not linking FLUKA and DPMJET-III. As shown in Fig. 7, the maximum energy deposition is 6% higher than that for the case of linking. The beam size is 0.2 mm in the comparison. Note that the difference becomes smaller as the beam size increases.

In addition to the above-mentioned beam parameters, other beam sizes have been studied depending on the beam energy. The maximum energy deposition in GeV/(cm^3 p) together with the corresponding specific energy deposition

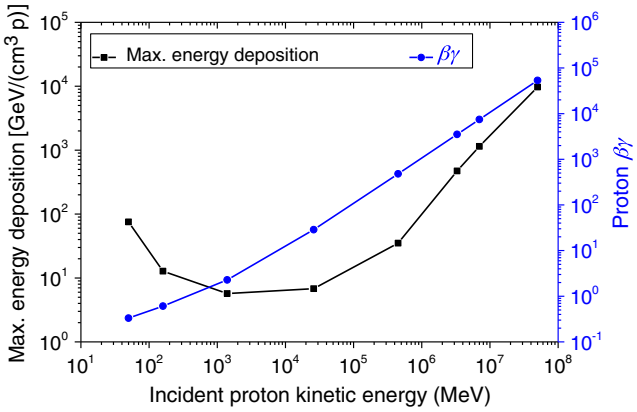

FIG. 6. Maximum energy deposition in copper as a function of the incident proton kinetic energy. The corresponding values of $\beta\gamma$ are plotted as well. The beam size is constant (0.2 mm) for the energies from 50 MeV to 50 TeV.

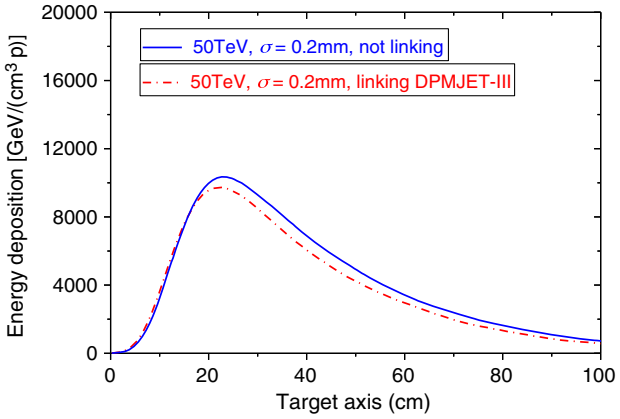

FIG. 7. Energy deposition of 50 TeV proton in copper along the target axis with and without linking FLUKA and DPMJET-III. Without linking, the maximum energy deposition is 6% higher than that for the case of linking.

of one nominal bunch in J/(g bunch) are listed in Table III. The bunch intensities listed in Table II were used to calculate the specific energy deposition. Note that, for both 50 and 160 MeV, a bunch intensity of 16.2×10^{11} was used. The locations of the maximums are shown as well. Three typical beam sizes were selected for each energy. In general, the maximum energy deposition grows nearly exponentially as the beam size decreases. Figure 8 shows the maximum energy deposition in copper as a function of the rms beam size for the energies from 50 MeV to 50 TeV. Note that the statistical error bar is shown for each simulation point, which might be hard to be identified because the relative error is always below 5%. Data in Table III give an integral map that enables us to predict the energy deposition behavior of protons in copper over a wide range of beam parameters.

C. Specific case study: Thin target

For beam-related machine protection, it is frequently needed to estimate the damage potentials of a target surface

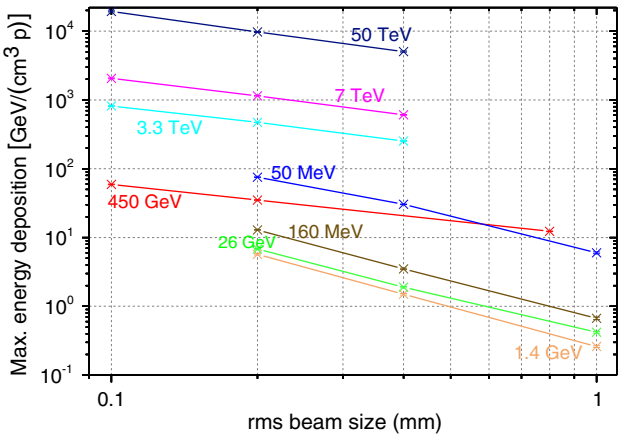

FIG. 8. Maximum energy deposition in copper as a function of the beam size for the energies from 50 MeV to 50 TeV.

TABLE III. Summary of the energy deposition of protons in a solid copper target with typical beam parameters.

Energy [GeV]	rms beam size [mm]	Maximum energy deposition [GeV/(cm^3 p)]	Maximum specific energy [J/(g bunch)]	Peak location [cm]
0.05	0.2	75.4	2181.2	0.39 (Bragg peak)
	0.4	30.4	879.4	0.39 (Bragg peak)
	1.0	6.0	173.6	0.39 (Bragg peak)
0.16	0.2	12.9	373.2	0.1
	0.4	3.5	101.3	0.3
	1.0	0.67	19.4	3.0 (Bragg peak)
1.4	0.2	5.7	164.9	0.2
	0.4	1.5	43.4	0.3
	1.0	0.26	7.5	0.4
26	0.2	6.8	16.4	0.3
	0.4	1.9	4.6	1.3
	1.0	0.42	1.0	4.2
450	0.1	59.2	121.6	11.0
	0.2	35.1	72.1	12.6
	0.8	12.3	25.3	15.8
3300	0.1	814.7	1454.8	15.8
	0.2	472.7	844.1	17.3
	0.4	252.9	451.6	18.3
7000	0.1	2059.1	4228.5	17.3
	0.2	1147.2	2355.9	18.8
	0.4	606.5	1245.5	19.8
50000	0.1	19326.6	34511.8	21.3
	0.2	9736.3	17386.3	22.3
	0.4	5043.6	9006.3	23.8

or a thin beam window which separates the vacuum of the beam line from a test area or beam dump block. To minimize the heating in a beam window and withstand the pressure difference, a supporting plate made of low-atomic-number materials with a thickness of typically a few millimeters (significantly smaller than one radiation length) is used. A very thin leak-tight foil made of materials with a low elastic modulus and thermal expansion coefficient (e.g., beryllium, copper, aluminum, titanium, and steel) is laid on the main plate to maintain the high vacuum of the beam line. For instance, a beam window consisting of a 5-mm-thick carbon-carbon (C-C) composite plate and a thin (0.254 mm) leak-tight beryllium foil has been used for the beam tests at the HiRadMat facility [34]. For the LHC beam dump entrance window, a 15-mm-thick C-C plate and a 0.2-mm-thick steel foil have been adopted [35].

For the estimation, it is common practice to calculate the energy loss of incident particles using the Bethe equation rather than performing a Monte Carlo simulation study. In this subsection, we examine the limits of the projectile energy and target thickness, within which the Bethe equation could still be applied without a significant loss

of accuracy. We compare the mean rate of electronic energy loss from the Bethe equation with the average energy deposited per unit length from FLUKA. The following Bethe equation was used to calculate the mean rate of electronic energy loss [36–39]:

$$-\frac{dE}{dx}_{\text{electronic}} = Kz^2\frac{Z}{A}\frac{1}{\beta^2}\left[\frac{1}{2}\ln\frac{2m_e c^2\beta^2\gamma^2 T_{\max}}{I^2} - \beta^2 - \frac{\delta(\beta\gamma)}{2}\right], \tag{1}$$

where $T_{\max}$ is the maximum kinetic energy that can be transferred to a free electron in a single collision, $\delta(\beta\gamma)$ is the density effect correction to ionization energy loss, and K and the other variables are defined in Table IV. $T_{\max}$ is further given by

$$T_{\max} = \frac{2m_e c^2\beta^2\gamma^2}{1 + 2\gamma(\frac{m_e}{M}) + (\frac{m_e}{M})^2}. \tag{2}$$

The density effect (reduction in the ionization loss) becomes increasingly significant due to the polarization of the medium above some high energy, which is usually computed exploiting Sternheimer's parameterization [40–42]:

$$\delta(\beta\gamma) = \begin{cases} 2(\ln 10)x - X & \text{if } x \geq x_1, \\ 2(\ln 10)x - X + a(x_1 - x)^k & \text{if } x_0 \leq x < x_1, \\ 0 & \text{if } x < x_0 \text{ (nonconductors)}, \\ \delta_0 10^{2(x-x_0)} & \text{if } x < x_0 \text{ (conductors)} \end{cases} \tag{3}$$

with $x = \log_{10}(p/Mc) = \log_{10}(\beta\gamma)$. Our motivation is mainly to check the applicability of the analytical approach in the practical case of thin targets while keeping its simplicity. Therefore, many corrections to the Bethe equation were not included, e.g., the radiative effect, which might have important contributions to the total energy loss of protons in medium and high-Z materials at very high energy. Table IV is a summary of variables used in this paper, including the definitions as well as values in the cases of solid copper and graphite targets irradiated by proton. Corresponding values in Ref. [43] were used for the coefficients in Eq. (3).

Combining Eqs. (1)–(3) with Table IV, we calculated the mean energy loss rate of one proton in copper, in units of MeV g^{-1} cm^2. No energy drop of the proton was considered, since we were studying a thin target. The energy loss per target length (in units of GeV/cm) was obtained by multiplying the mean energy loss rate from the Bethe equation by the solid copper density.

In FLUKA, a short cylindrical copper target was used. We spanned the radius (4 cm, which was large enough to stop any secondary particle from escaping the target transversely) in one bin and the length (1 cm) in 100 bins. Note that the rms beam size used in the simulation was

TABLE IV. Summary of the variables used in this paper.

Symbol	Definition	Units or value for copper	Units or value for graphite
K	$4\pi N_A r_e^2 m_e c^2$	0.307075 MeV mol^{-1} cm^2	
z	Charge number of the projectile particle	1 for a proton	
$m_e c^2$	Electron mass $\times c^2$	0.511 MeV	
M	Incident particle mass	938.26 MeV/c^2 for a proton	
p	Incident particle momentum $p = M\beta\gamma c$	MeV/c	
N_A	Avogadro's number	6.022×10^{23} mol^{-1}	
r_e	Classical electron radius $e^2/4\pi\varepsilon_0 m_e c^2$	2.818×10^{-15} m	
Z	Charge number of the target material	29	6
A	Atomic mass of the target material	63.546 g/mol	12.0107 g/mol
ρ	Density of the target material	8.96 g/cm^3	2.28 g/cm^3
I	Mean excitation energy of target atom	322 eV	78 eV
a	Sternheimer's parameter for certain Z	0.14339	0.20762
k	Sternheimer's parameter for certain Z	2.9044	2.9532
x_0	Sternheimer's parameter for certain Z	−0.0254	−0.009
x_1	Sternheimer's parameter for certain Z	3.2792	2.4817
X	Sternheimer's parameter for certain Z	4.4190	2.8926
δ_0	Sternheimer's parameter for certain Z	0.08	0.14

0.2 mm. In this way, the normalized energy deposition of each transverse cross section at a certain longitudinal position could be exported directly from FLUKA. Multiplying the normalized energy deposition by the area of the cross section, the energy deposited per unit length in GeV/cm at that position was obtained, which is independent of the beam size. The average energy deposited per target length as a function of the target thickness was computed by increasing the number of longitudinal bins that were taken into account.

A comparison of the energy deposition or loss rate in GeV/cm between FLUKA simulations and analytical calculations is shown in Fig. 9. The results from the simulation corresponding to three target thicknesses are shown. When the target thickness is 0.01 cm, differences between the simulation results and direct analytical values are small even at the highest energy of 50 TeV. As the target thickness increases from 0.1 to 0.3 cm, the energy loss rate is more and more underestimated by the Bethe equation, especially at higher energies, because of the development of the hadron shower. At 50 MeV, a large difference between the simulation and analysis can be seen in the case of the target thickness of 0.3 cm, due to a large proportion of energy drop. It is appropriate to estimate the damage potential of a copper surface or submillimeter-thick copper foil using directly the Bethe equation besides FLUKA.

The energy loss rate at low energies ($\beta\gamma \ll 1$) is high, because the effective interaction time allows for a higher momentum transfer from incident protons to target electrons. With growing projectile energy, the momentum transfer decreases, and, since the energy transfer increases slowly, the minimum of energy loss rate is observed.

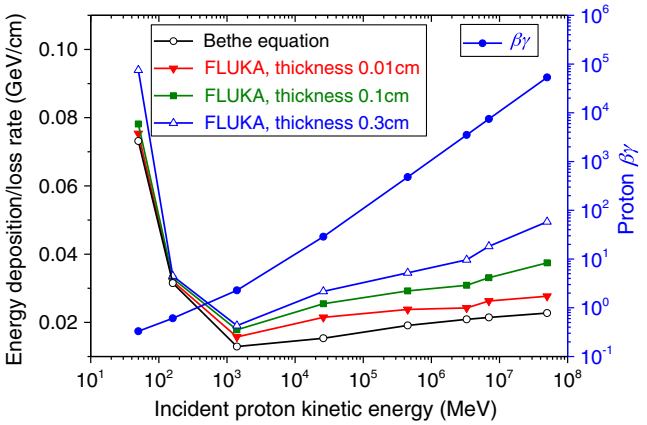

FIG. 9. Energy deposition or loss rate per proton in a thin copper target as a function of kinetic energy ranging from 50 MeV to 50 TeV. Comparisons are made between FLUKA simulations (energy deposition per target length) and direct calculations using the Bethe equation (energy loss rate). For the simulation results, three target thicknesses are considered as denoted in the figure.

For $\beta\gamma = 2$–3, the incident proton could transfer <0.5% of its energy to the target electrons. In the energy region $2\gamma m_e/M \gg 1$, the maximum transferred energy can be simplified to $T_{\max} \approx c^2\beta^2\gamma M$; i.e., almost all the energy of the primary proton could be transferred to the electrons [44].

The conclusions following from the analysis of Bethe equation and Fig. 9 help understand the results for the total maximum energy deposition in the copper target presented in Fig. 6. For energies up to 26 GeV, the maximum energy deposition is dominated by primary protons because of the above-mentioned momentum transfer effect. At 450 GeV, the maximum energy transferred to an electron approaches $T_{\max} \approx 30\%$ of the primary proton energy and keeps rapidly growing with increasing $\beta\gamma$; therefore, a significant part of the target electrons get accelerated and form so-called delta rays. The delta rays also deposit energy into the target material. Besides, secondary projectiles start playing a significant role at high energies. All these effects add up and give an increasing energy deposition at high energies as observed in Fig. 6.

D. Specific energy deposition of bunched beam

In Sec. III B, we have presented the energy deposition per proton in a solid copper target. In this part, the specific energy deposition of a certain number of protons will be discussed to illustrate the beam impact on accelerator equipment made of copper. Of particular concern is assessing the number of protons needed to melt and even evaporate copper. The melting energy and boiling energy were estimated using the nonconstant specific heat capacity as a function of the temperature. According to the estimation, 674 J/g is needed to melt copper from 300 K and 6250 J/g to evaporate it, taking into account the latent heat of melting (207 J/g) and vaporization (4730 J/g). As a comparison, the melting energy and boiling energy become 614 and 5913 J/g, respectively, if a constant specific heat capacity of 0.385 J/(g K) is adopted. It is worth mentioning that there are many superconducting components working at very low temperatures like 1.9 K, especially at high-energy accelerators. Here we consider that the initial copper temperature is always 300 K to have a conservative damage estimation from the viewpoint of machine protection. Note that the specific energy needed to increase the copper temperature from 1 to 300 K is about 79 J/g.

The number of protons required to melt the copper material at the location of maximum energy deposition (denoted as $n_{\mathrm{p,max}}$) as well as at the entrance of the target (denoted as $n_{\mathrm{p,entrance}}$) are listed in Table V. Moreover, the corresponding number of proton bunches (denoted as $N_{\mathrm{p,max}}$ and $N_{\mathrm{p,entrance}}$, respectively) are presented as well, based on the bunch intensity listed in Table II. As a first approximation, the heat propagation is ignored during the irradiation period from the first bunch to the last bunch.

TABLE V. Number of protons and proton bunches needed to melt copper at the maximum energy deposition point as well as at the target front surface.

Energy [GeV]	rms beam size [mm]	$n_{p,\mathrm{max}}$	$N_{p,\mathrm{max}}$	$n_{p,\mathrm{entrance}}$	$N_{p,\mathrm{entrance}}$
0.05	0.2	5.0×10^{11}	0.3	1.3×10^{12}	0.8
	0.4	1.2×10^{12}	0.8	5.1×10^{12}	3.2
	1.0	6.3×10^{12}	3.9	3.1×10^{13}	18.9
0.16	0.2	2.9×10^{12}	1.8	3.0×10^{12}	1.9
	0.4	1.1×10^{13}	6.7	1.2×10^{13}	7.5
	1.0	5.6×10^{13}	34.8	7.3×10^{13}	44.8
1.4	0.2	6.6×10^{12}	4.1	6.8×10^{12}	4.2
	0.4	2.5×10^{13}	15.5	2.5×10^{13}	15.5
	1.0	1.5×10^{14}	89.6	1.5×10^{14}	89.6
26	0.2	5.6×10^{12}	41.1	6.0×10^{12}	44.4
	0.4	2.0×10^{13}	147.2	2.2×10^{13}	159.8
	1.0	9.0×10^{13}	665.7	1.1×10^{14}	822.3
450	0.1	6.4×10^{11}	5.5	1.4×10^{12}	11.9
	0.2	1.1×10^{12}	9.4	5.0×10^{12}	43.8
	0.8	3.1×10^{12}	26.7	6.7×10^{13}	586.1
3300	0.1	4.6×10^{10}	0.5	1.4×10^{12}	13.7
	0.2	8.0×10^{10}	0.8	4.1×10^{12}	40.6
	0.4	1.5×10^{11}	1.5	1.3×10^{13}	134.8
7000	0.1	1.8×10^{10}	0.2	1.3×10^{12}	10.9
	0.2	3.3×10^{10}	0.3	4.1×10^{12}	35.7
	0.4	6.2×10^{10}	0.5	1.5×10^{13}	131.3
50000	0.1	2.0×10^{9}	0.02	6.9×10^{11}	6.9
	0.2	3.9×10^{9}	0.04	3.3×10^{12}	32.7
	0.4	7.5×10^{9}	0.07	1.1×10^{13}	113.3

It should be noted that for 50 and 160 MeV, the beam size is most likely a few millimeters in normal operation, where the maximum energy deposition is actually an order of magnitude lower than for the beam sizes in the table. The small beam sizes are studied for completeness; for example, in Fig. 5, energy deposition along the target axis was shown while a constant beam size of 0.2 mm was used for all the energies from 50 MeV to 50 TeV. An interesting feature that can be found in Table V is that the target surface can withstand up to hundreds of bunches before melting, even though less than one bunch is able to melt the copper at the maximum energy deposition point above 3.3 TeV. As explained in Sec. II, it is reasonable to consider a nominal beam size of about 0.8 mm for the SPS when it operates as an injector of the LHC. From Table V, it can be concluded that the highest beam intensity to avoid melting is about 3.1×10^{12}, which agrees well with the damage test experiments performed with the 450 GeV proton beam extracted from the SPS [45]. Analogously, the melting threshold is 3.3×10^{10} for the beam size of 0.2 mm at the LHC top energy of 7 TeV and 2.0×10^{9} for 0.1 mm at the FCC top energy of 50 TeV, as shown in Table V. Note that the estimations were made according to the local energy deposition values based on the mentioned binning. Therefore, the considered material volumes were rather small, in the range of $4 \times 10^{5} - 6 \times 10^{8}$ $\mu\mathrm{m}^3$. From the viewpoint of machine protection, it is important to know when the material begins melting. However, the melting of a small volume of material inside the target might be regarded as undesirable but not necessarily unacceptable. Specific situation analysis needs to be performed on a case-by-case basis. It is also worth mentioning that in some accident cases the intense heat loads on the targets (e.g., on the collimator jaw) in a very short time can generate a thermal shock with a rapid increase of the target temperature which may cause a local deformation (mechanical damage) before reaching the melting point of the material. This phenomenon has been studied to check the robustness of the LHC collimators as reported in Ref. [46].

The specific energies of one bunch with 1.0×10^{11} protons as well as of one full FCC beam with 10600 bunches are plotted in Figs. 10(a) and 10(b), respectively. The proton energy is 50 TeV, and the beam size of 0.2 mm is used. In Fig. 10(a), a maximum of about 17390 J/g can be found, which is almost 3 times the boiling energy 6250 J/g, meaning that one bunch of protons with the mentioned parameters is sufficient not only to melt a portion of the copper target but also to evaporate the material around the location of the maximum energy deposition. The melting and boiling regions are from $L = 4.2$ cm to $L = 110$ cm and from $L = 9.9$ cm to $L = 55.3$ cm, respectively. Figure 10(b) illustrates that the penetration depth (the deepest location where copper is melted) of the full beam in copper is at least 295 cm, since here the energy deposition is calculated only by FLUKA (static approximation); i.e., the hydrodynamic tunneling effect is not considered, or, equivalently, the beam energy is assumed to be deposited instantaneously. The full impact of the FCC beam with a bunch train on a solid copper target considering hydrodynamic tunneling is beyond the scope of this paper. A detailed study can be found in Ref. [27].

The above estimations of a beam impact on copper are direct applications of the simulated energy deposition. As a first approximation, the local deposited heat is obtained by simply multiplying the energy deposition per proton by the total number of protons, neglecting the bunch structure and density change of the material. From the machine protection point of view, such linear scaling is meaningful, since a large margin of safety is usually adopted concerning the beam impact on the accelerator components. For example, a beam of very limited damage potential with 5.0×10^{8} protons at 50 TeV or 1.0×10^{10} protons at 3.3 TeV is recommended for FCC-hh commissioning [47], based on the data listed in Table V. We remark that an accurate analysis of beam interaction with matter must rely on a multidisciplinary approach coupling different numerical tools, especially for high-energy and high-intensity beams.

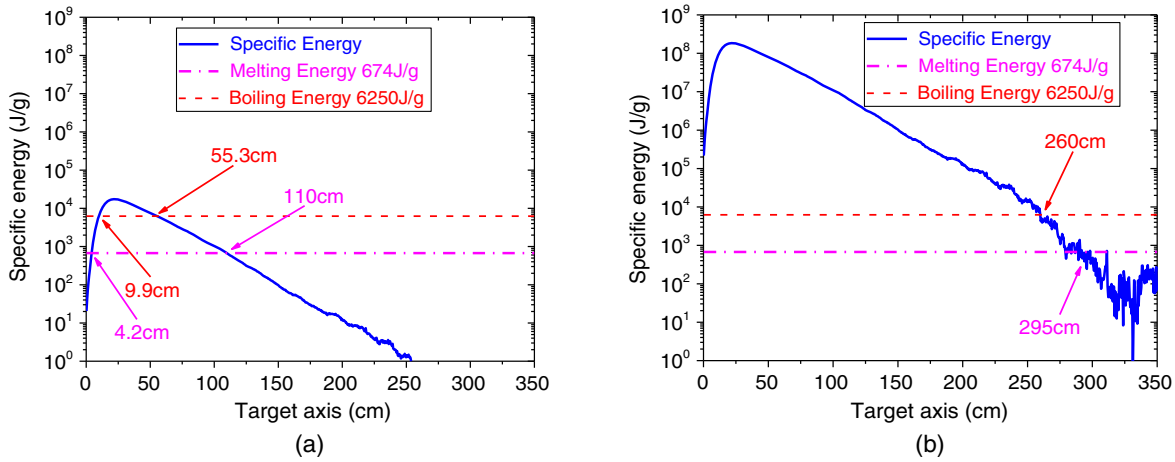

FIG. 10. Specific energies of (a) one bunch with 1.0×10^{11} protons and (b) one full FCC beam with 10600 bunches. The top energy of the FCC (50 TeV) is used. The beam size is 0.2 mm.

As illustrated in Ref. [48], the dynamic response is generally classified into an elastic regime, a plastic regime, and a shock wave regime. It has been shown that the severity of the response is proportional to the deposited power density and to the duration of the interaction. The type of dynamic response can be approximately predicted according to the total specific energy deposited in the target, regardless of the actual material. As pointed out in Ref. [48], the dynamic response will for most cases remain within the elastic regime, if the deposited energy is below 100 J/cm^3. Accelerator components are usually designed to work in this regime. Between 100 J/cm^3 and 10 kJ/cm^3, the plastic dynamic response is expected to occur. Both the elastic regime and plastic regime can be treated using standard finite element tools relying on implicit time-integration schemes like ANSYS. In Table V, the proton number and bunch number were determined to make the local specific energy below 674 J/g (the melting energy), which equals 6 kJ/cm^3. It implies that the plastic dynamic response is expected. Once the deposited energy exceeds 10 kJ/cm^3, the stress waves will be strong enough to generate major changes of density and extensive damage to the material, resulting in a dynamic response in the shock wave regime. The impacted metal material will usually experience phase transitions with the formation of liquid, gas, and even plasma or even be physically displaced in the region of the impact. In the case of a long bunch train, the subsequent bunches will penetrate deeper and deeper along the target as the upstream density has been reduced gradually. The energy deposition range extends especially in the longitudinal direction, while the energy deposition (per proton) in the upstream part is reduced. As already mentioned, this effect is called hydrodynamic tunneling. As shown in Fig. 10, the energy deposited by one 50 TeV bunch already exceeds 10 kJ/cm^3 in a considerable part of the target, implying that the shock wave regime is reached. To analyze the dynamic response within the shock wave regime, hydrocodes with explicit time-integration schemes must be employed, such as ANSYS-Autodyn, LS-Dyna, and BIG2, which make use of complex material constitutive models. Once the relative density change is substantial, e.g., >15%, a modified distribution of the energy deposition (from FLUKA, MARS, or Geant4) is needed as input for the following dynamic simulation.

IV. ENERGY DEPOSITION OF PROTON IN SOLID GRAPHITE

In the previous section, copper was chosen as a target material, since it is frequently used in the accelerator components such as magnets and beam screens, as well as for a comparison with the existing damage test results. Of considerable interest is a similar study with graphite as a target material, because graphite is widely used in the accelerator machine protection systems, for example, in collimators, beam absorbers, and beam dump blocks. In this section, we report the corresponding studies for a solid graphite target in a similar way. The longitudinal bin size was 0.003 cm at 50 MeV, 0.05 cm at 160 MeV, 0.1 cm at 1.4 GeV, 0.25 cm at 26 GeV, and 0.5 cm at 450 GeV and all higher energies.

The two-dimensional energy deposition distributions of one proton corresponding to a beam size of $\sigma = 0.2$ mm at 50 MeV and 50 TeV are plotted in Figs. 11(a) and 11(b), respectively. Compared to the case of copper target as shown in Fig. 2, the particle cascades penetrate much deeper in the graphite target, whereas the energy deposition reduces dramatically. For example, the Bragg peak moves from 0.39 cm for a copper target to deeper than 1 cm for a graphite target at 50 MeV. The different behavior is due to the difference between the number of electrons (function of the charge number, density, and mass number) in the two materials. For 50 MeV and 50 TeV protons in graphite, the energy deposition along the target axis is plotted in

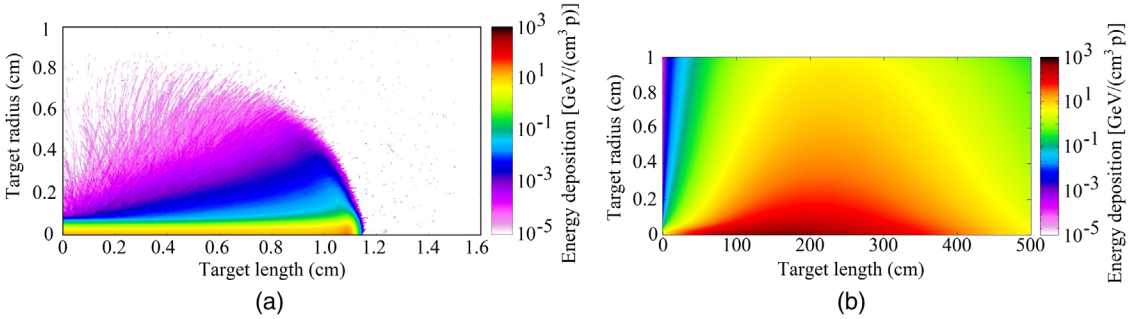

FIG. 11. Two-dimensional energy deposition in units of $\mathrm{GeV/cm^3}$ per proton in a solid graphite target at the energies of (a) 50 MeV and (b) 50 TeV. The rms beam size is $\sigma = 0.2$ mm.

Figs. 12(a) and 13(a), respectively. The radial energy deposition at the longitudinal positions where we have the maximum on-axis energy deposition is shown in Figs. 12(b) and 13(b). At 50 MeV, the Bragg peaks lie at $L = 1.09$ cm for the three beam sizes of 0.2, 0.4, and 1.0 mm, with the peak values of 25.0, 10.6, and 2.3 $\mathrm{GeV/(cm^3\,p)}$, respectively, which are approximately one-third of the corresponding values in the case of copper (Fig. 3). For 50 TeV, the peaks are much wider than that in Fig. 4. The maximum energy deposition for the beam size

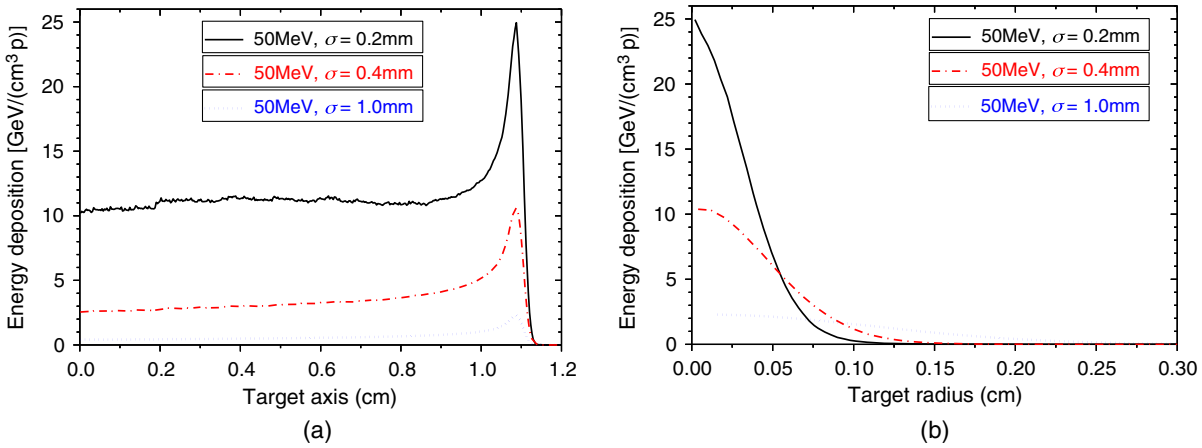

FIG. 12. Energy deposition per 50 MeV proton in a cylindrical graphite target for three different beam sizes of 0.2, 0.4, and 1.0 mm (a) in the longitudinal direction at $r = 0$ and (b) in the radial direction at $L = 1.09$ cm (position of the Bragg peaks).

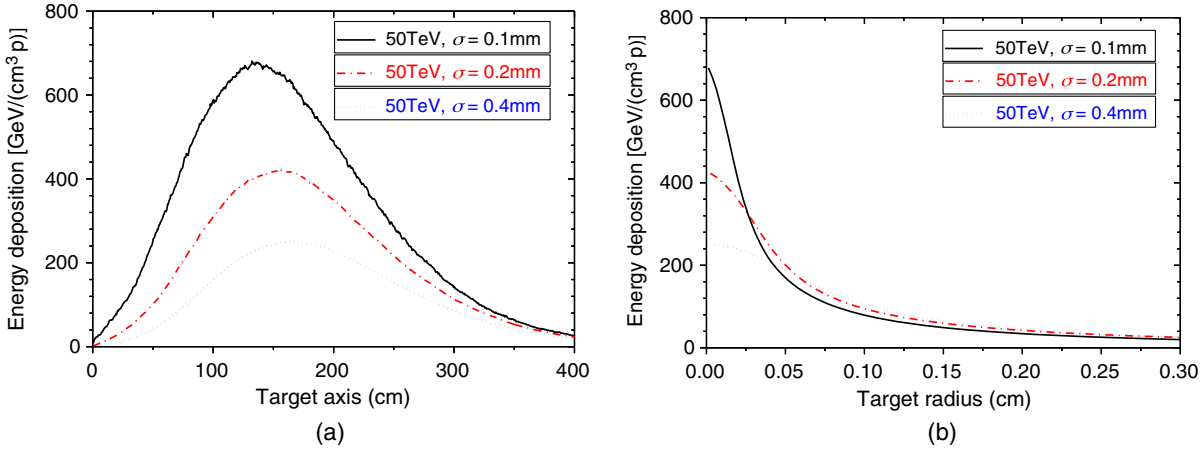

FIG. 13. Energy deposition per 50 TeV proton in a cylindrical graphite target for three different beam sizes (a) in the longitudinal direction at $r = 0$ and (b) in the radial direction at $L = 135.8$ cm for the beam size of 0.1 mm, $L = 155.3$ cm for 0.2 mm, and $L = 164.3$ cm for 0.4 mm.

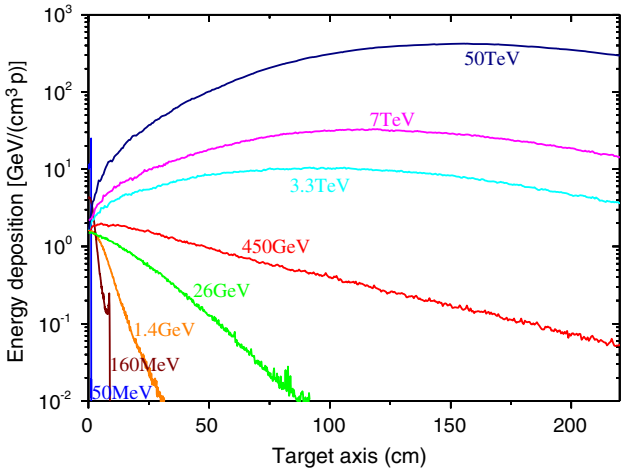

FIG. 14. Energy deposition per incident proton as a function of the depth into the solid graphite target at $r = 0$. The beam size is 0.2 mm for all the presented energies from 50 MeV to 50 TeV.

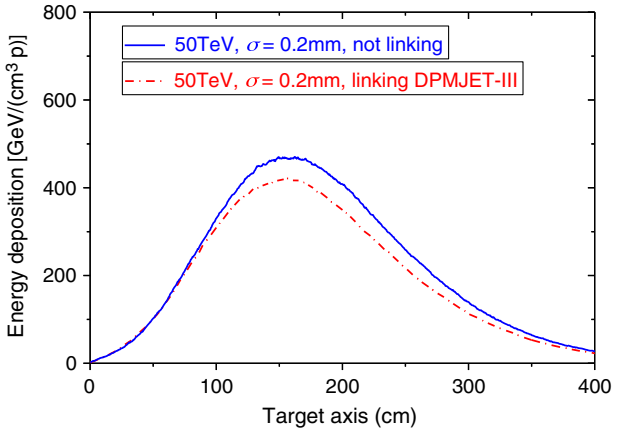

FIG. 16. Energy deposition of 50 TeV proton in graphite along the target axis with and without linking FLUKA and DPMJET-III. Without linking, the maximum energy deposition is 11% higher than that for the case of linking.

of 0.1 mm is 678.2 GeV/(cm^3 p) at $L = 135.8$ cm, for 0.2 mm, 422.9 GeV/(cm^3 p) at $L = 155.3$ cm, and for 0.4 mm, 250.9 GeV/(cm^3 p) at $L = 164.3$ cm, which are about 20 times lower than that in the case of a copper target. Similar to Fig. 5, Fig. 14 shows the energy deposition per proton in graphite along the target axis at various energies with the same beam size of 0.2 mm. It can be seen that the Bragg peaks appear only at 50 and 160 MeV and disappear at higher energies due to energy deposited by secondary particles. For both 1.4 and 26 GeV, the maximum energy deposition lies very close to the entrance. The maximum moves from 5.3 to 155.3 cm, as the energy increases from 450 GeV to 50 TeV. The peak energy deposition of a proton in graphite as a function of the energy is shown in Fig. 15. It can be seen that the curve has a flatter bottom compared to that in Fig. 6 with a minima of 1.5 GeV/(cm^3 p) at 26 GeV ($\beta\gamma = 28.7$). It is explained by the lower energy deposition from the delta rays, since the

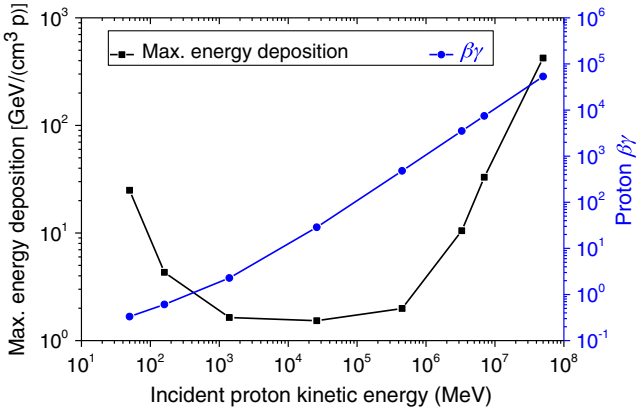

FIG. 15. Maximum energy deposition in graphite as a function of the incident proton kinetic energy. The corresponding values of $\beta\gamma$ are plotted as well. The beam size is 0.2 mm for all the presented energies from 50 MeV to 50 TeV.

number of influenced electrons is ~4 times lower in carbon than in copper.

The energy deposition along the target axis was also simulated for a 50 TeV proton in graphite while not linking FLUKA and DPMJET-III. As shown in Fig. 16, the maximum energy deposition is 11% higher than that for the case of linking when the beam size is 0.2 mm.

Three beam sizes were studied for each energy in the case of a graphite target like in the case of copper. The maximum energy deposition in GeV/(cm^3 p) as well as the corresponding specific energy deposition of one nominal bunch in J/(g bunch) are listed in Table VI. The positions of the maxima are presented as well. They move deeper into the target as the beam size increases for a given proton energy as long as there is no Bragg peak. Such a phenomenon can be observed in Table III as well. This is due to the development of the hadronic shower as illustrated in Ref. [49]. In principle, the integral of energy deposition over the transverse cross section is independent of the beam size, as long as the target radius is large enough to stop particles escaping transversely. For the spatial distribution of energy deposition, the beam size plays a crucial role. In the case of a pencil beam (on the assumption that all protons concentrate at a single impact point; i.e., the transverse beam size is zero), the maximum energy deposition occurs at the very beginning due to proton ionization in a null volume, which is thus infinite by definition. For a broad high-energy beam, the maximum energy deposition is due to the electromagnetic shower developed from proton nuclear reactions (i.e., due to the secondary particles other than beam protons). Depending on the beam energy and the target material, its longitudinal position moves from the target surface to a certain maximum depth as the beam size increases from zero to infinite. In Figs. 2(b) and 11(b), it can be seen that the maximum energy deposition along the target (at a fixed

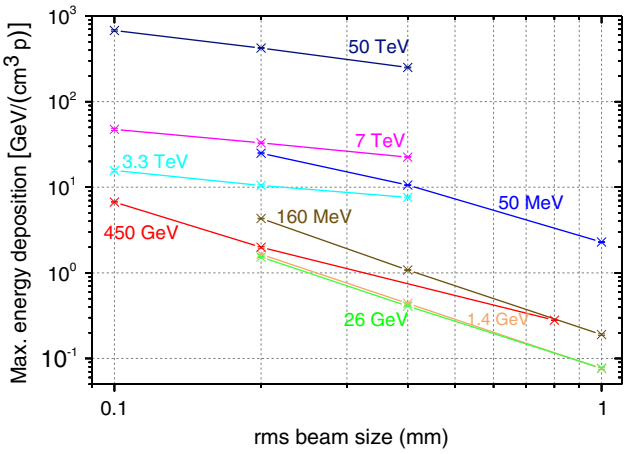

FIG. 17. Maximum energy deposition in graphite as a function of the beam size for the energies from 50 MeV to 50 TeV.

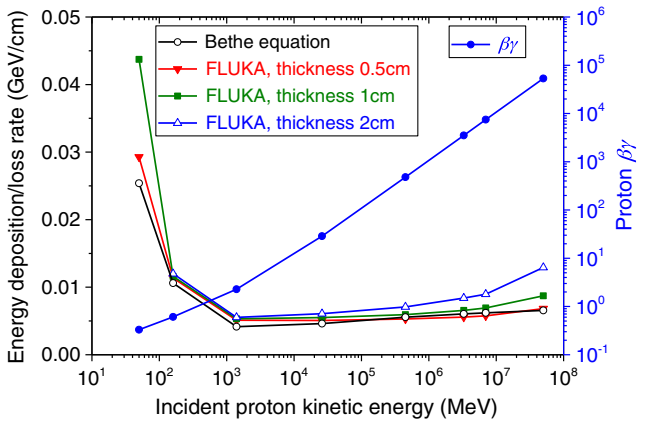

FIG. 18. Energy deposition or loss rate per proton in a thin graphite target as a function of kinetic energy ranging from 50 MeV to 50 TeV. Comparisons are made between FLUKA simulations (energy deposition per target length) and direct calculations using the Bethe equation (energy loss rate). For the simulation results, three target thicknesses are considered as denoted in the figure.

radius) appears at a deeper location as the radius increases. For a beam with a bigger transverse beam size, there are more protons further away from the beam center (target axis). Their contributions to the on-axis energy deposition lead to a deeper peak compared to the near-axis protons. As a result, the integrated energy deposition along the target axis shows a deeper peak when the beam size is bigger. Figure 17 shows the maximum energy deposition in graphite as a function of the rms beam size for the energies from 50 MeV to 50 TeV. The very small statistical error bar is shown for each simulation point. These representative data in Tables III and VI allow us to estimate rapidly and conveniently the beam impacts on different accelerator components over a variety of beam parameters.

For the energy deposition or loss rate as a function of the proton energy, a comparison between FLUKA and the Bethe equation is made in Fig. 18 in the same way as in Fig. 9. Related variables for graphite are listed in Table IV. We spanned the target radius (2 cm) in one bin and the target length (2 cm) in 40 bins. A smaller target radius was used compared to the case of copper, since the energy deposition decays faster along the radius in a graphite target, while the same rms beam size of 0.2 mm was used as for copper. The simulated results corresponding to three target thicknesses of 0.5, 1, and 2 cm are shown. Differences between simulation results and analytical values are very small when the target thickness is 0.5 cm or even 1 cm, unless at 50 MeV, due to the large proportion of energy drop after a few millimeters. When the target thickness is 2 cm, the difference between the simulation results and analytical values increases as the proton energy increases because of the electromagnetic shower. The energy loss rate of 50 MeV protons for the target thickness of 2 cm is not presented, since the interaction depth is less than 1.2 cm as shown in Fig. 11(a). It can be concluded that the damage capability of protons in subcentimeter-thick graphite plates can be well estimated directly by using the Bethe equation.

TABLE VI. Summary of the energy deposition of protons in a solid graphite target with typical beam parameters.

Energy [GeV]	rms beam size [mm]	Maximum energy deposition [GeV/(cm^3 p)]	Maximum specific energy [J/(g bunch)]	Peak location [cm]
0.05	0.2	25.0	2836.4	1.09 (Bragg peak)
	0.4	10.6	1206.2	1.09 (Bragg peak)
	1.0	2.3	260.3	1.09 (Bragg peak)
0.16	0.2	4.3	490.0	0.08
	0.4	1.1	122.8	0.63
	1.0	0.19	21.6	0.28
1.4	0.2	1.6	186.4	0
	0.4	0.44	50.0	0.56
	1.0	0.08	8.6	0.81
26	0.2	1.5	14.5	0.63
	0.4	0.41	3.9	1.4
	1.0	0.08	0.7	3.4
450	0.1	6.7	54.2	3.3
	0.2	2.0	16.1	5.3
	0.8	0.28	2.3	49.3
3300	0.1	15.7	110.2	42.3
	0.2	10.5	73.7	91.8
	0.4	7.6	53.5	110.3
7000	0.1	47.5	383.3	98.3
	0.2	33.0	266.3	119.8
	0.4	22.5	181.6	130.3
50000	0.1	678.2	4759.3	135.8
	0.2	422.9	2967.8	155.3
	0.4	250.9	1760.7	164.3

V. CONCLUSIONS AND FUTURE WORKS

The energy deposition of protons in solid copper and graphite targets was analyzed with the help of numerical simulations carried out through the well-developed Monte Carlo program FLUKA, taking into account the typical values of the beam energy and beam size for the hadron accelerator complex at CERN. The proton energy varied from 50 MeV to 50 TeV. Three representative beam sizes were studied for each energy. Different energy loss behaviors of protons in copper and graphite targets were explored and compared, in terms of the range and maximum values of the energy deposition. Comparisons of the energy deposition or loss rate between FLUKA and the Bethe equation were performed. The results showed that the damage potential of subcentimeter-thick graphite target and submillimeter-thick copper foil can be well estimated directly by the Bethe equation, because the energy drop of the primary proton is generally small (special attention should be paid to the initial proton energy of 50 MeV) and the hadron shower has not developed extensively.

Based on the data matrix obtained in this paper, one can rapidly predict the energy deposition properties for any other beam parameter including the beam energy and beam size within an extensive range. For instance, the proposed HE-LHC will reach a beam energy of 16.5 TeV, of which the maximum energy deposition can be estimated to be around 3000 $\mathrm{GeV}/(\mathrm{cm}^3\,\mathrm{p})$ at a depth of 20 cm in the solid copper target when the beam size is 0.2 mm. Therefore, beam impacts on accelerator components can be evaluated as a consequence of expected and unexpected beam losses. These results allow us to calculate the maximum allowed number of incident protons or bunches to keep the copper target temperature below a certain limit, for example, the melting point.

For the FCC, at an injection energy of 3.3 TeV, one bunch is sufficient to melt the copper at the location of the maximum energy deposition. At the top energy of 50 TeV, one bunch can even evaporate a certain volume of copper in the target. Furthermore, the minimum penetration depth into the copper target for a certain beam can be predicted as well using the static approximation, as explained in Sec. III. Note that the hydrodynamic tunneling was not considered, which may lead to a significant lengthening of the particle penetration depth in the case of a long bunch train at high energies. This phenomenon was confirmed by the dedicated HiRadMat experiment and can be simulated by coupling FLUKA with proper hydrodynamic codes such as BIG2 and ANSYS on a case-by-case basis. For the sake of more general interest, we have summarized the existing relevant studies on the hydrodynamic tunneling effect, which were reported by some of us with collaborators. Other specific case studies on hydrodynamic tunneling will be performed especially for FCC, coupling FLUKA and BIG2 (or ANSYS Autodyn). Besides, as a future work, the grazing impact of high-energy and high-intensity proton beams on accelerator components like beam screens will be studied as well.

Such a study is of critical importance, as it is able to serve as a reference for a quick assessment of the beam impacts on the accelerator elements that are made of copper or graphite. Further analysis can be carried out using it as a starting point. These results should be useful not only for the CERN accelerators but also for other relevant proton accelerators.

ACKNOWLEDGMENTS

The authors thank Francesco Cerutti, Anton Lechner, and Roberto Cevenini for the help with the FLUKA code and the computing cluster. We also thank Naeem A. Tahir from GSI, Germany for helpful discussions and our colleagues Andrzej Siemko and Markus Zerlauth for a very careful reading of the paper. The FCC study has received funding from the European Union's Horizon 2020 research and innovation programme under Grant Agreement No. 654305 (EuroCirCol).

[1] M. Benedikt, D. Schulte, and F. Zimmermann, Optimizing integrated luminosity of future hadron colliders, Phys. Rev. ST Accel. Beams **18**, 101002 (2015).

[2] R. Assmann, R. Bailey, O. Brüning, O. Dominguez, G. Rijk, J. M. Jimenez, S. Myers, L. Rossi, L. Tavian, E. Todesco, and F. Zimmermann, Report No. CERN-ATS-2010-177, 2010.

[3] B. List, L. Hagge, and N. J. Walker, Change management at the International Linear Collider ILC, in *Proceedings of the 7th International Particle Accelerator Conference, IPAC-2016, Busan, Korea, 2016* (JACoW, Busan, Korea, 2016), p. 3835.

[4] R. Corsini, Status and future of the CLIC study, in *Proceedings of the 26th International Linear Accelerator Conference, LINAC-2012, Tel-Aviv, Israel, 2012* (JACoW, Tel-Aviv, Israel, 2012), p. 719.

[5] Y. W. Wang, S. Bai, H. P. Geng, T. J. Bian, X. H. Cui, D. Wang, J. Gao, and Y. S. Zhu, A preliminary design of the CEPC interaction region, in *Proceedings of the 7th International Particle Accelerator Conference, IPAC-2015, Richmond, VA, 2015* (IEEE, Richmond, VA, 2015), p. 2019.

[6] F. Zimmermann, M. Benedikt, D. Schulte, and J. Wenninger, Challenges for highest energy circular colliders, in *Proceedings of the 5th International Particle Accelerator Conference, IPAC-2014, Dresden, Germany, 2014* (JACoW, Geneva, 2014), p. 1.

[7] D. Schulte, FCC-hh machine layout and optics, in *FCC Week 2016* (Roma, Italy, 2016).

[8] R. Schmidt, R. Assmann, E. Carlier, B. Dehning, R. Denz, B. Goddard, E. B. Holzer, V. Kain, B. Puccio, B. Todd, J. Uythoven, J. Wenninger, and M. Zerlauth, Protection of the CERN Large Hadron Collider, New J. Phys. **8**, 290 (2006).

[9] R. B. Appleby, B. Goddard, A. Gomez-Alonso, V. Kain, T. Kramer, D. Macina, R. Schmidt, and J. Wenninger, Beam-related machine protection for the CERN Large Hadron Collider experiments, Phys. Rev. ST Accel. Beams **13**, 061002 (2010).

[10] D. C. Wilson, C. A. Wingate, J. C. Goldstein, R. P. Godwin, and N. V. Mokhov, Hydrodynamic calculations of 20-TeV beam interactions with the SSC beam dump, in *Proceedings of the 15th Particle Accelerator Conference, PAC-1993, Washington, DC, 1993* (IEEE, New York, 1993), p. 3090.

[11] N. A. Tahir, R. Schmidt, M. Brugger, R. Assmann, A. Shutov, I. V. Lomonosov, V. E. Fortov, A. R. Piriz, C. Deutsch, and D. H. H. Hoffmann, Interaction of Super Proton Synchrotron beam with solid copper target: Simulations of future experiments at HiRadMat facility at CERN, Nucl. Instrum. Methods Phys. Res., Sect. A **606**, 186 (2009).

[12] N. A. Tahir, R. Schmidt, M. Brugger, R. Assmann, A. Shutov, I. V. Lomonosov, V. Gryaznov, A. R. Piriz, S. Udrea, D. H. H. Hoffmann, and C. Deutsch, Generation of warm dense matter and strongly coupled plasmas using the High Radiation on Materials facility at the CERN Super Proton Synchrotron, Phys. Plasmas **16**, 082703 (2009).

[13] N. A. Tahir, R. Schmidt, A. Shutov, I. V. Lomonosov, V. Gryaznov, A. R. Piriz, C. Deutsch, and V. E. Fortov, The Large Hadron Collider and the Super Proton Synchrotron at CERN as tools to generate warm dense matter and non-ideal plasmas, Contrib. Plasma Phys. **51**, 299 (2011).

[14] N. A. Tahir, V. Kain, R. Schmidt, A. Shutov, I. V. Lomonosov, V. Gryaznov, A. R. Piriz, M. Temporal, D. H. H. Hoffmann, and V. E. Fortov, The CERN Large Hadron Collider as a Tool to Study High-Energy Density Matter, Phys. Rev. Lett. **94**, 135004 (2005).

[15] N. A. Tahir, B. Goddard, V. Kain, R. Schmidt, A. Shutov, I. V. Lomonosov, A. R. Piriz, M. Temporal, D. H. H. Hoffmann, and V. E. Fortov, Impact of 7-TeV/c large hadron collider proton beam on a copper target, J. Appl. Phys. **97**, 083532 (2005).

[16] N. A. Tahir, R. Schmidt, M. Brugger, A. Shutov, I. V. Lomonosov, A. R. Piriz, and D. H. H. Hoffmann, Simulations of full impact of the Large Hadron Collider beam with a solid graphite target, Laser Part. Beams **27**, 475 (2009).

[17] N. A. Tahir, R. Schmidt, A. Shutov, I. V. Lomonosov, A. R. Piriz, D. H. H. Hoffmann, C. Deutsch, and V. E. Fortov, Large Hadron Collider at CERN: Beams generating high-energy-density matter, Phys. Rev. E **79**, 046410 (2009).

[18] N. A. Tahir, J. B. Sancho, A. Shutov, R. Schmidt, and A. R. Piriz, Impact of high energy high intensity proton beams on targets: Case studies for Super Proton Synchrotron and Large Hadron Collider, Phys. Rev. ST Accel. Beams **15**, 051003 (2012).

[19] The official FLUKA site, http://www.fluka.org/.

[20] T. T. Böhlen, F. Cerutti, M. P. W. Chin, A. Fassò, A. Ferrari, P. G. Ortega, A. Mairani, P. R. Sala, G. Smirnov, and V. Vlachoudis, The FLUKA code: Developments and challenges for high energy and medical applications, Nucl. Data Sheets **120**, 211 (2014).

[21] A. Ferrari, P. R. Sala, A. Fassò, and J. Ranft, Reports No. CERN-2005-10, No. INFN/TC_05/11, and No. SLAC-R-773, 2005.

[22] N. A. Tahir, J. B. Sancho, R. Schmidt, A. Shutov, and A. R. Piriz, Prospects of warm dense matter research at HiRadMat facility at CERN using 440 MeV SPS proton beam, High Energy Density Phys. **9**, 269 (2013).

[23] N. A. Tahir, F. Burkart, A. Shutov, R. Schmidt, D. Wollmann, and A. R. Piriz, Simulations of beam-matter interaction experiments at the CERN HiRadMat facility and prospects of high-energy-density physics research, Phys. Rev. E **90**, 063112 (2014).

[24] R. Schmidt, J. B. Sancho, F. Burkart, D. Grenier, D. Wollmann, N. A. Tahir, A. Shutov, and A. R. Piriz, First experimental evidence of hydrodynamic tunneling of ultra–relativistic protons in extended solid copper target at the CERN HiRadMat facility, Phys. Plasmas **21**, 080701 (2014).

[25] F. Burkart, R. Schmidt, V. Raginel, D. Wollmann, N. A. Tahir, A. Shutov, and A. R. Piriz, Analysis of 440 GeV proton beam–matter interaction experiments at the High Radiation Materials test facility at CERN, J. Appl. Phys. **118**, 055902 (2015).

[26] N. A. Tahir, Hydrodynamic tunneling and machine protection problem in Future Circular Collider, *FCC Week 2016, Roma, Italy, 2016*, https://indico.cern.ch/event/438866/contributions/1084920/.

[27] N. A. Tahir, F. Burkart, R. Schmidt, A. Shutov, D. Wollmann, and A. R. Piriz, Beam induced hydrodynamic tunneling in the Future Circular Collider components, Phys. Rev. Accel. Beams **19**, 081002 (2016).

[28] E. Boltezar, H. Haseroth, W. Pirkl, G. Plass, T. R. Sherwood, P. H. Standley, P. Têtu, U. Tallgren, D. Warner, and M. Weiss, Review and status of the CERN new 50 MeV linac project, in *Proceedings of the 1976 Proton Linear Accelerator Conference, Chalk River, Ontario, Canada, 1976*, p. 45.

[29] F. Gerigk and M. Vretenar, Reports No. CERN-AB-2006-084 ABP/RF and No. CARE-Note-2006-022-HIPPI, 2006.

[30] R. Garoby, S. Hancock, and J. L. Vallet, Demonstration of bunch triple splitting in the CERN PS, in *Proceedings of the 7th European Particle Accelerator Conference, Vienna, 2000* (EPS, Geneva, 2000), p. 304.

[31] B. Mikulec, A. Blas, C. Carli, A. Findlay, K. Hanke, G. Rumolo, and J. Tan, Report No. CERN-ATS-2009-070, 2009.

[32] S. Roesler, R. Engel, and J. Ranft, The Monte Carlo event generator DPMJET-III, in *Proceedings of Monte Carlo 2000 Conference, Lisbon, Portugal, 2000*, edited by A. Kling, F. Barão, M. Nakagawa, L. Távora, and P. Vaz (Springer-Verlag Berlin, 2001), p. 1033.

[33] R. Schmidt, Introduction to machine protection, in *Proceedings of the 2014 Joint International Accelerator School on Beam Loss and Accelerator Protection, Newport Beach, 2014*, edited by R. Schmidt (CERN, Geneva, 2016), p. 14.

[34] M. Monteil, J. Blanco, and R. Veness, A transparent vacuum window for high-intensity pulsed beams, Vacuum 2011) 1165 ,**85**).

[35] R. Veness, B. Goddard, L. Massidda, S. J. Mathot, and A. Presland, Design of the LHC beam dump entrance window, in *Proceedings of the 10th European Particle Accelerator Conference, Edinburgh, Scotland, 2006* (EPS-AG, Edinburgh, Scotland, 2006), p. 1792.

[36] H. A. Bethe, Zur theorie des durchgangs schneller korpuskularstrahlen durch materie, Ann. Phys. (Berlin) **397**, 325 (1930).

[37] H. A. Bethe, Bremsformel fuer elektronen relativistischer geschwindigkeit, Z. Phys. **76**, 293 (1932).

[38] F. Bloch, Bremsvermoegen von Atomen mit mehreren Elektronen, Z. Phys. **81**, 363 (1933).

[39] K. A. Olive *et al.* (Particle Data Group), Review of particle physics, Chin. Phys. C **38**, 090001 (2014).

[40] R. M. Sternheimer, The density effect for the ionization loss in various materials, Phys. Rev. **88**, 851 (1952).

[41] R. M. Sternheimer and R. F. Peierls, General expression for the density effect for the ionization loss of charged particles, Phys. Rev. B **3**, 3681 (1971).

[42] R. M. Sternheimer, M. J. Berger, and S. M. Seltzer, Density effect for the ionization loss of charged particles in various substances, At. Data Nucl. Data Tables **30**, 261 (1984).

[43] http://pdg.lbl.gov/AtomicNuclearProperties/.

[44] S. P. Denisov, Ionization energy loss of charged particles, Soros. Obrazov. Zh. **11**, 90 (1999).

[45] V. Kain, J. B. Sancho, M. Brugger, and M. Sapinski, Beam induced damage – what is a safe beam?, in *Proceedings of Chamonix 2009 Workshop on LHC Performance, Chamonix, France, 2009* (Chamonix, 2009), p. 171.

[46] A. Bertarelli, O. Aberle, R. W. Assmann, S. Calatroni, A. Dallocchio, T. Kurtyka, M. Mayer, R. Perret, S. Redaelli, and G. Robert-Demolaize, Mechanical design for robustness of the LHC collimators, in *Proceedings of the 21st Particle Accelerator Conference, Knoxville, TN, 2005* (IEEE, Piscataway, NJ, 2005), p. 913.

[47] L. Ponce, FCC-hh instrumentation overview and challenges, in *FCC Week 2017, Berlin, Germany, 2017*.

[48] A. Bertarelli, Beam-induced damage mechanisms and their calculation, in *Proceedings of the 2014 Joint International Accelerator School on Beam Loss and Accelerator Protection, Newport Beach, United States, 2014*, edited by R. Schmidt (CERN, Geneva, 2016), pp. 159–227.

[49] A. Lechner, Energy deposition in collimator/dump materials: challenges due to the energy increase to 50 TeV, in *FCC Week 2015, Washington DC 2015* (2015).